ACS APPLIED MATERIALS & INTERFACES

Research Article

www.acsami.org

Interconnected V_2O_5 Nanoporous Network for High-Performance Supercapacitors

B. Saravanakumar,[†] Kamatchi K. Purushothaman,[‡] and G. Muralidharan*[,§]

[†]Faculty of Physics, Mahalingam College of Engineering and Technology, Pollachi, Tamilnadu, India

[‡]Faculty of Physics, TRP Engineering College (SRM Group), Irungalur, Trichy, Tamilnadu, India

[§]Department of Physics, Gandhigram Rural University, Gandhigram, Tamilnadu, India

Supporting Information

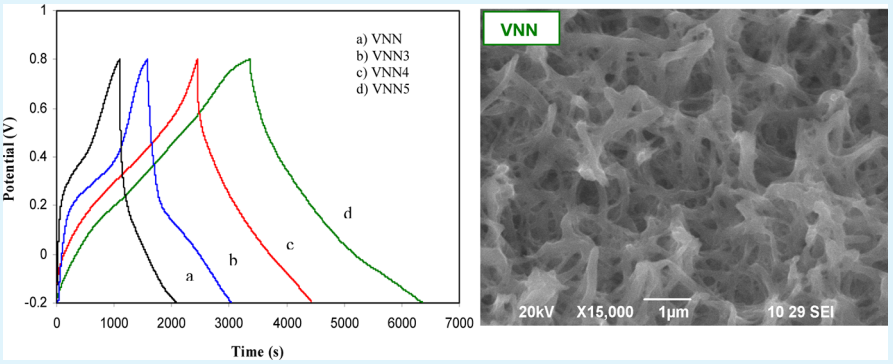

ABSTRACT: Vanadium pentoxide (V_2O_5) has attracted attention for supercapcitor applications because of its extensive multifunctional properties. In the present study, V_2O_5 nanoporous network was synthesized via simple capping-agent-assisted precipitation technique and it is further annealed at different temperatures. The effect of annealing temperature on the morphology, electrochemical and structural properties, and stability upon oxidation−reduction cycling has been analyzed for supercapacitor application. We achieved highest specific capacitance of 316 F g^{-1} for interconnected V_2O_5 nanoporous network. This interconnected nanoporous network creates facile nanochannels for ion diffusion and facilitates the easy accessibility of ions. Moreover, after six hundred consecutive cycling processes the specific capacitance has changed only by 24%. A simple cost-effective preparation technique of V_2O_5 nanoporous network with excellent capacitive behavior, energy density, and stability encourages its possible commercial exploitation for the development of high-performance supercapacitors.

KEYWORDS: *nanoporous V_2O_5, supercapacitor, aqueous electrolyte, K^+ ions*

1. INTRODUCTION

The present day technological society demands energy storage devices for various portable electronic devices and hybrid motor vehicles. In this regard, batteries of different kinds and high-performance capacitors are the focus of current scientific research. Supercapacitors (SCs) are investigated because of their unique features like high power density (10 kW kg^{-1}), long cycle life (>1 × 10^5), excellent reversibility (90−95%), lack of maintenance, operational safety.[1] They require very simple circuit for charging. The supercapacitors find use in a range of applications including consumer electronics (cameras, mobile phones, video recorders, toys, etc.,), medical applications, electrical utilities, transportation, and military/defense systems. SCs can be coupled with fuel cells or batteries to deliver high power to recover energy during braking.[2] The electrochemical capacitors (ECs) can be classified as electrochemical double layer capacitor (EDLC) and pseudocapacitors. EDLC based on the separation of charges at the interface between the electrode and electrolyte. The pseudocapacitor utilizes the fast Faradic process involving reversible electrochemical redox reactions.[3] The redox reaction occurs at the electrode−electrolyte interface and it is the major component that leads to energy storage.

The improvement of surface-dependent processes promotes the overall energy storage. Electrode materials are to be tailored with more intercalation sites or fast diffusion pathways to achieve this goal.[4] At nanometer scale, keeping the facile contact areas and fully realizing the advantage of electrode material is still a challenge.[5] Recently more attention has been devoted to the synthesis and evaluation of nanoporous materials for they can integrate morphological features like high surface area, porosity and good conductivity. These materials provide a new pathway to solve the problem by shortening the ion diffusion distance as a result of reduced dimension of the particles. The continuous porous network creates channels for better ion transport to the redox-active material.[6,7] The high degree of pore connectivity in nanoporous

Received: January 22, 2012
Accepted: August 22, 2012
Published: August 22, 2012

network enhances the mass transport and also increases the material lifetime in energy storage applications.[8] Hence fabrication and use of nanoporous network structures for supercapacitor applications are expected to provide high capacitance values coupled with excellent performance. Functional nanostructured metal oxides are considered as excellent electrode material in terms of achieving high specific capacitance.[9] Among transition metal oxides, hydrous ruthenium oxide/activated carbon ($RuO_x.nH_2O$/AC) in acidic electrolyte is reported to be an excellent electrode material because of its high specific capacitance, 1580 F g^{-1}, and better electrochemical stability.[10] The commercial use of this novel material is limited because of its high cost and toxicity. Hence good efforts are being made toward exploration, improvement, and discovery of new electrode material such as MnO_2,[11] NiO,[12] and CO_3O_4[13] to achieve supercapacitors with better electrochemical characteristics. In this context, vanadium pentoxide (V_2O_5) has been widely studied over the past decade since the first report by Whittingham et al.,[14] Among the low cost metal oxides, V_2O_5 is a favorable candidate as a supercapacitor electrode because of its most accessible layered structure, high specific capacity, mixed oxidation states (V^{2+},V^{3+},V^{4+}, and V^{5+}), low cost, easy procedure for synthesis and nontoxic chemical properties.[15] To obtain different nanostructures of V_2O_5 many techniques such as hydrothermal,[16] electrospinning,[17] sol–gel,[18] template-assisted growth[19] and various other methods are used. Neutral aqueous electrolytes in supercapacitor possess low cost, high ionic conductivity, and nonflammability. K^+ ions have smallest hydrated ionic radius and highest ionic conductivity (0.33 nm, 72.2 cm^2/Ω mol) compared to Li^+ (0.38 nm, 38.6 cm^2/Ω mol) and Na^+ (0.358 nm, 50.1 cm^2/Ω mol).[20,21] Therefore, SCs based on environmental benign K_2SO_4 electrolyte is expected to exhibit good electrochemical properties.

The broad industrial applications of nano structured metal oxides are limited due to complicated processing methods and expensive fabrication. For commercial applications a low cost, easy and one step synthesize procedure are preferable for mass production. In this study, we report a simple, low-temperature (100 °C), cost-effective method based on capping-agent-assisted precipitation technique to synthesize V_2O_5 nanoporous network and investigate the potential of the material for supercapacitor applications in a nontoxic aqueous electrolyte.

2. EXPERIMENTAL SECTION

2.1. Synthesis of V_2O_5 Nanoporous Network. Analytical grade vanadium pentoxide (V_2O_5), hydrogen peroxide (30% H_2O_2) and K_2SO_4 were purchased from SD Fine Chemicals Ltd., India. Disodium citrate ($Na_2HC_6H_5O_7$) was purchased from Sigma Alrich, India. All chemicals were used as such without further purification. In a typical synthesis process, about 1.7733 g of V_2O_5 was added in to 375 mL of deionized water, followed by slow dropping of 15 mL of 30% H_2O_2 solution (15 mL/min). The decomposition of H_2O_2 initiated many simultaneous chemical reactions as described in the literature[22]

$$V_2O_5 + 4H_2O_2 \rightarrow 2[VO(O_2)_2(OH_2)]^- + 2H^+ + H_2O \quad (1)$$

$$V_2O_5 + 3H_2O_2 + 3H_2O \rightarrow 2[VO(O_2)(OH_2)_3]^+ + O_2 \quad (2)$$

$$2[VO(O_2)_2(OH_2)]^- + 4H^+ + 2H_2O \rightarrow 2[VO(O_2)(OH_2)_3]^+ + O_2 \quad (3)$$

$$2[VO(O)_2(OH_2)_3]^+ \rightarrow 2[VO_2]^+ + O_2 + 6H_2O \quad (4)$$

After mixing of V_2O_5 powder with H_2O_2 and deionized water (DI), the resulting yellow slurry bubbled vigorously with color change to orange(exothermic reaction). The color change was attributed to formation of diperoxovanadate anion $[VO(O_2)_2(OH_2)]^-$. After a few minutes, the solution changed to transparent ruby red color suggesting the presence of the red monoperoxovanadate cation $[VO(O_2)_2(OH_2)_3]^+$ and further diaxovanadium cation $[VO_2]^+$ was formed. The solution was prepared using concentrated H_2O_2 (30%). Because of this, gelation will start readily within few minutes.[23] To avoid this, disodium citrate was added immediately as capping agent under vigorous magnetic stirring at ambient temperature. The solution is stirred for 5 h to form a homogeneous solution and aged for 3 days. The products were collected by centrifugation and dried at 100 °C for 10 h in an oven to get final product. The prepared sample was annealed at different temperatures 300, 400, and 500 °C for 1 h.

2.2. Characterization Techniques. As synthesized powders were characterized by X-ray diffraction (XRD) using a PANalytical X'pert-PRO diffractometer equipped with Cu Kα sealed tube (λ = 1.5406 Å). The sample was scanned in the range between 10 and 70° with a step size of 0.02° and exposure time of 10 s. FTIR spectra have been recorded using Perkin-Elmer Spectrum BX-II spectrophotometer using KBr pellets at room temperature. Multipoint nitrogen adsorption–desorption experiments were performed using Micrometeritics ASAP 2020 analyzer using Brunauer–Emmett–Teller (BET) gas adsorption method at 77K. The porosity distribution of the samples were generated from desorption branch of the isotherm using the Barrett–Joyner–Halenda (BJH) method. The powder morphology and structure of the materials were investigated by scanning electron microscopy (JEOL JSM 3690 scanning electron microscope) and transmission electron microscopy (TEM-Philips JEOL CM12). Cyclic voltammetry (CV), galvanostatic charge–discharge, and electrochemical impedance spectroscopy (EIS) measurements were carried out using CHI 660 D electrochemical workstation (CH Instruments).

2.3. Fabrication of Electrodes and Evaluation. Electrochemical investigations of V_2O_5 nanoporous network were performed using a three-electrode cell, which consists of the prepared V_2O_5 as the working electrode, platinum wire as counter electrode, and Ag/AgCl as the reference electrode. A syrup of the electrode material was prepared by blending 85 wt % V_2O_5, 10 wt % activated carbon (Sigma-Aldrich), and 5 wt % polytetrafluoroethylene (Sigma-Aldrich) with a few drops of ethanol. This slurry mixture was coated on to a 1 cm^2 nickel foil surface. It was followed by drying at 80 °C for 8 h to obtain the working electrode. The electrochemical analysis was carried out in 0.5 M K_2SO_4 aqueous electrolyte solution at room temperature.

The specific capacitance (C, in F g^{-1}) of the active material in the electrode can be calculated using the relation

$$C = \frac{i}{mv} \quad (5)$$

Where i (mA) is the average current, m (mg cm^{-2}) is the mass of the electrode active material, and v is the voltage sweep rate.

The specific capacitance was determined using charge–discharge curves as well, by applying the following equation

$$C = \frac{I\Delta t}{m\Delta v} \quad (6)$$

Where I (mA) is the discharge current, Δt (s) is the time required for discharge, and ΔV (V) is the discharge potential. The specific capacitance values reported for all samples have been calculated using the active mass of V_2O_5 in the working electrode.

The energy density values were obtained from CV analysis. The energy density values were calculated using the equation

$$E = \frac{1}{2}CV^2 \quad (7)$$

where C is the specific capacitance at a particular scan rate within the potential window of 1 V.

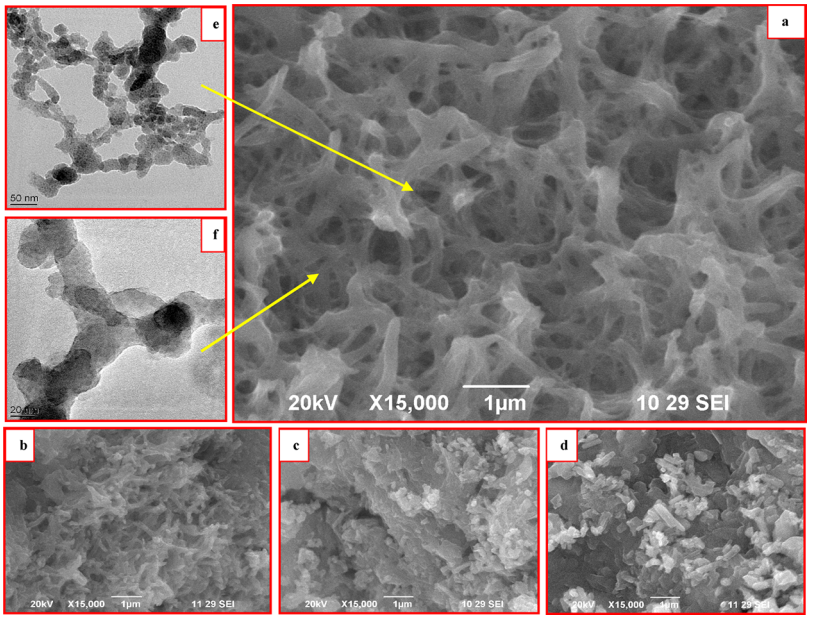

Figure 1. (a) SEM image of the V_2O_5 nanoporous network (VNN); (b) VNN annealed at 300 °C ;(C) VNN annealed at 400 °C; (d) VNN annealed at 500 °C; (e, f) TEM images of VNN.

3. RESULTS AND DISCUSSION

3.1. Morphological Studies. Morphology of the material significantly influences the suitability of the material for supercapacitor application. A representative scanning electron microscopy (SEM) image of as synthesized V_2O_5 powder (Figure 1a) shows a intimately interconnected network like structure. The image confirms that the surface texture of the material is having many small and large pores. The Transmission electron micrograph (TEM) images (Figure 1e, f) further confirm the porous nature of the material and interconnections between pores. The organized porous nano structures create nanochannels and allow more efficient ion diffusion for energy storage.[24] Presence of the large pores enables rapid electrolyte transport, whereas the small pores with nanosize effectively increase the area available for electrochemical reactions. Such results have been reported by Chen et.al.[25] After the material is annealed at 300 °C for 1 h, crystallization of the material seems to have started as the voids between the network (pores) appear to shrink (Figure 1b). Further increase in annealing temperature (400 °C), leads to rapid disappearance of pores and the aggregation of the material could be observed in Figure 1c. As the temperature of annealing is increased to 500 °C, the nanoporous network structure of the material completely collapses and the surface turns into rough surfaces (Figure 1d). The aggregation of V_2O_5 networks at temperatures greater than 300 °C leads to the collapsing of the nanoporous network.

3.2. X-ray Diffraction Analysis. The crystal structure formation of V_2O_5 nanoporous network (VNN) and annealed at 300,400 and 500 (denoted as VNN3, VNN4, and VNN5, respectively) were determined by XRD and diffraction patterns are shown in (Figure 2). The absence of sharp diffraction peaks and poor intensity of XRD patterns for as prepared and V_2O_5 annealed at 300 °C suggests to be poor crystallinity. Further the presence of (001), (101), and (110) for VNN4 and VNN5 confirms highly crystalline nature of the material with orthorhombic structure (JCPDS Card No. 41−1426). This can be indexed as Shcherbianite system with space group of

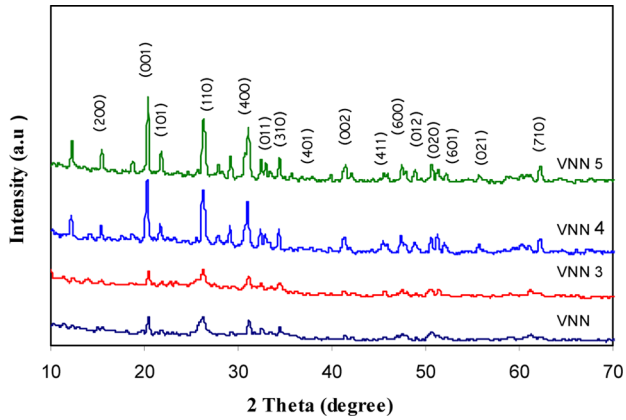

Figure 2. XRD patterns recorded for VNN, VNN3, VNN4, and VNN5.

Pmn(59) and cell parameters are a = 1.151 nm, b = 3.565 nm, and c = 4.372 nm. The average particle size obtained from Debye−Scherrer method indicted that the particle size grows from 46 nm (VNN4) to 55 nm (VNN5).

3.3. FTIR Spectra Analysis. FTIR spectra (Figure 3) of as synthesized orthorhombic V_2O_5 and annealed with different temperatures were recorded to ensure the structure of V_2O_5. In all cases, the spectra exhibited characteristic IR bands corresponding to V_2O_5.The band at 1018 cm^{-1} is attributable to V═O stretching mode while the band at 742 cm^{-1} could be assigned to V−OH_2 stretching mode due to coordinated water content.[5] The 1665 cm^{-1} band is the well-known O−H bending mode of vibration due to the residual water content in the material.[26] The absence of 1665 cm^{-1} band in the spectra for annealed samples indicates the removal of the residual water.

3.4. BET Analysis. The N_2 adsorption−desorption isotherms of VNN, VNN3, VNN4, and VNN5 samples are shown in panels a and b in Figure 4. The insets are showing corresponding BJH pore size distribution profile. The isotherm of all samples show a sharp capillary condensation step at high

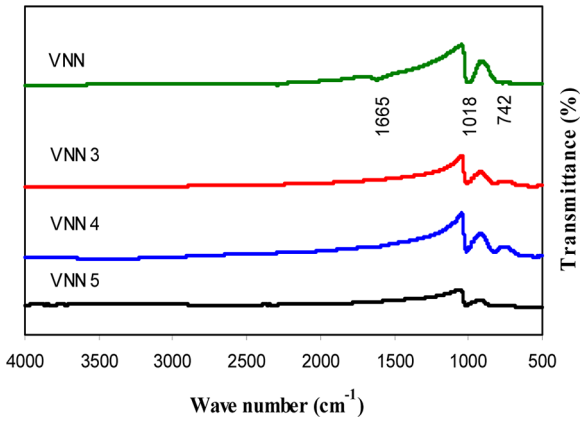

Figure 3. FTIR spectra for VNN, VNN3, VNN4, and VNN5.

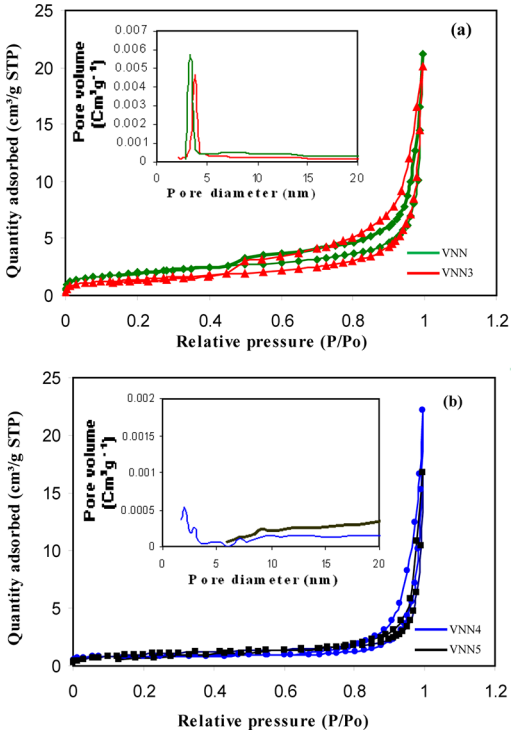

Figure 4. (a) Nitrogen adsorption−desorption isotherms of VNN and VNN3 samples. (b) Isotherms of VNN4 and VNN5 samples. The insets of both figures show the pore-size distribution of samples, respectively.

relative pressure and belongs to type IV isotherm according to IUPAC classification.[27] The isotherms of all samples show hysteresis loop at p/p^{o} values between 0.45 to 0.99. This confirms the presence of high degree of meso pores in the samples.[28,29] The pore size distribution profiles of all samples are calculated using BJH model. The pore size distribution maxima of sample VNN is well balanced at 3.75 nm, which is most favorable for ion diffusion in energy storage applications. Pore size in the range of 2−50 nm is encouraging to improve the capacitive behavior of the electrode material due to facile access of ions into the electrode active materials.[1] The pore size distribution maxima of VNN decreases from 3.75 to 3.35 nm for the sample annealed at 300 °C (VNN3). The pore size distribution of VNN4 centered at 1.82 and 2.92 nm. Though, the pore size of 1.82 nm does not facilitate efficient redox reactions in energy storage applications.[30] In addition to these observations an interesting fact in pore size distribution analysis is note worthy. The pore size of VNN continuously decreases in the pore size distribution (PSD) data over increase of annealing temperature. The pores present in the material are likely to decrease in width (or) merge together to form bigger grains. Further, no well-resolved pore size distribution maxima could be observed for the samples annealed at 500 °C (VNN5), probably because of the reduction in nanopores due to aggregation. These observations provide clear indication that the increase of annealing temperature induces the shrinkage of pores and turn in to grains. The BET specific surface area of the VNN, VNN3, VNN4 and VNN5 samples, respectively, are 7.1, 4.9, 3.7, and 2.8 m^2/g. A reduction in specific surface area of samples could be observed with increase of annealing temperature. From the pore size and BET surface area analysis, it can be expressed that VNN samples possess porous morphology with meso pores. This meso porosity is very significant and supposed to make better electrolyte penetration through their nano channels and improve the specific capacitance and performance. The results obtained from pore size, BET analysis confirms the shrinkage of pores with increase of annealing temperature.

3.5. Electrochemical Studies. *3.5.1. Cyclic Voltammetry Study.* To explore the potential application of the material for supercapacitor, we characterized the electrodes by cyclic voltammograms (CVs). Figure 5a shows a typical CV curves of VNN and annealed at various temperatures within the potential range from 0 to 1 V (Versus Ag/AgCl) in 0.5 M K_2SO_4 at scan rate of 2 mV s^{-1}. The electrochemical K^+ insertion process occurring at V_2O_5 electrodes can be expressed as

$$V_2O_5 + xK^+ + xe^- \leftrightarrow K_xV_2O_5 \quad (8)$$

where x is the mole fraction of inserted K^+ ions. The maximum specific capacitance of 316 F g^{-1} was obtained for as prepared samples without annealing. This high specific capacitance value attributed to involvement of V_2O_5 in Faradic redox reaction contributes the pseudocapacitance share increased the specific capacitance. The specific capacitance decreases from 316 to 135 F g^{-1} as annealing temperature increases to 300 °C. Further the down trend of specific capacitance was observed for samples annealed at 400 °C (95 F g^{-1}) and 500 °C (90 F g^{-1}). Similarly, the decrease of specific capacitance from 181 F g^{-1} (VNN) to 75 (VNN3), 67 (VNN4), and 35 (VNN5) at scan rate of 5 mVs^{-1} was also observed in Figure S1 (Supporting Information). This decreasing tendency of specific capacitance can be understood by correlation of SEM micrographs. The micrographs and XRD patterns clearly indicate the closing of pores and growth of the grains. The networks seem to close in. This shrinkage of nanoporous network morphology of the sample reduces the routes for diffusion of charges. From SEM it is seen that large pores with unagglomarated chains are present in the unannealed samples. Pore size analysis also confirms the shrinkage of pores during increase of annealing temperature. The CV curves of as prepared sample for different voltage sweep rate from 2 to50 mV s^{-1} is presented in Figure 5b. The anodic current was found to decrease with increasing scan rate. At higher scan rate, the surface of active material is not completely accessed by ions .The diffusion of electrolyte ions limited by high current, and at lower scan rate, the inner active sites or pores of electrode active material is effectively used for charge storage and this leads to high capacitance.[31,32] Increase in scan rate influences the quasi- rectangular shape of the CV

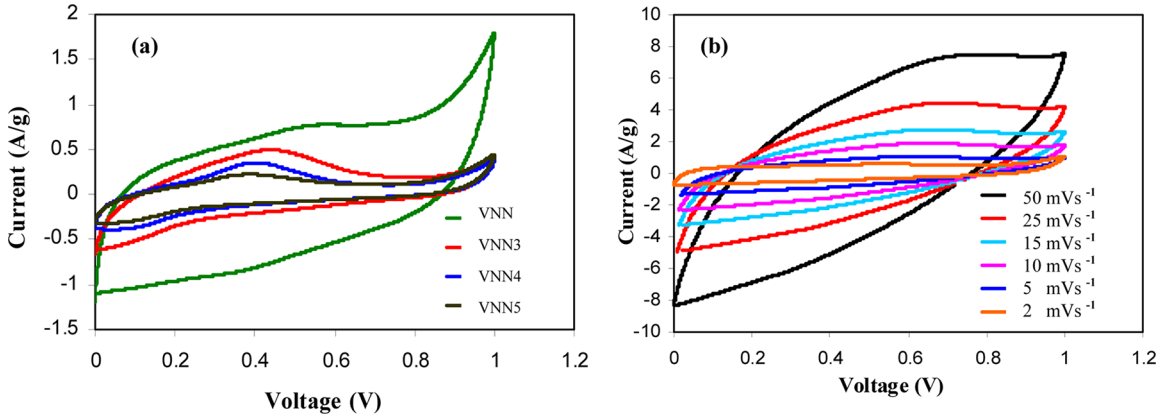

Figure 5. (a) CV curves for VNN, VNN3, VNN4, and VNN5 measured at 2 mV s^{-1} in 0.5 M K2SO4 electrolyte. (b) CV curves of VNN electrode measured at different scan rates.

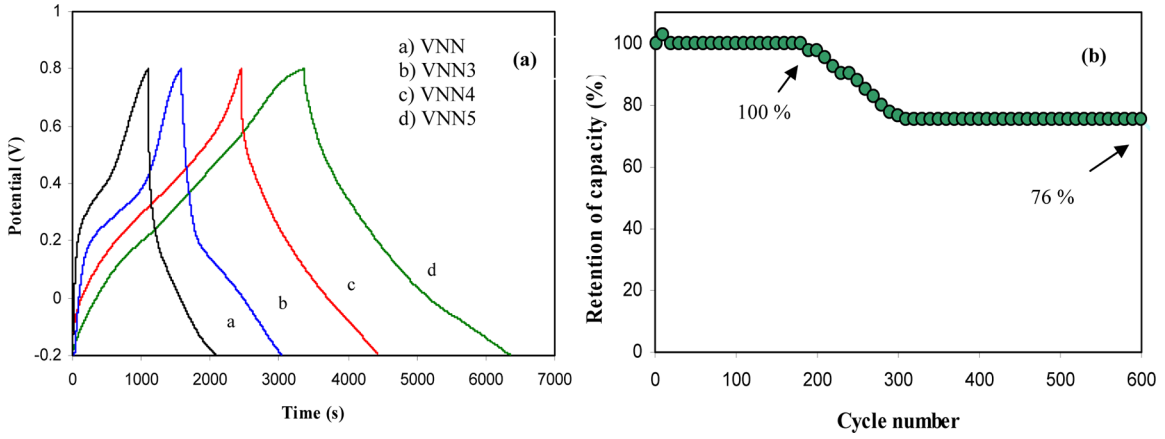

Figure 6. (a) Charge/discharge curves for VNN, VNN3, VNN4, and VNN5 measured at 100 mA g^{-1}. (b) Cycling behavior of VNN measured at 1000 mA g^{-1}.

curves. The retention of the shape of CV curves at higher scan rates is a good indication of better reversibility. The variation of anodic peak current density with scan rate is shown in Figure S2 in the Supporting Information. Almost a linear relationship has been observed. This indicates the contribution of surface redox reaction in the pesudocapacitive behavior of the electrodes.[28]

3.5.2. Galvanostatic Charge–Discharge Study. Galvanostatic charge/discharge (GCD) experiments were performed to estimate the specific capacitance and to understand the sustainability of this material as supercapacitor electrodes. The GCD curves are plotted at current density of 100 mA g^{-1} between 0.2 to 0.8 V (Figure 6a). Slight curvature in all charge–discharge curves illustrates the supercapacitor behavior is influenced by electrical double layer contributions (EDLC) along with the redox reactions (Pseudocapacitor).[33] Specific capacitance values determined using the charge/discharge technique are found to be 304 F g^{-1} (VNN), 187 F g^{-1} (VNN3), 141 F g^{-1} (VNN4) and 92 F g^{-1} (VNN5). Small variation was observed in specific capacitances of the samples determined by GCD and CV. This can be explained by the actuality that the value of specific capacitance measured by CV is one particular potential, at the same time that obtained by GCD is a average capacitance over the potential range of 0.2 to 0.8 V. Averaging the capacitances in a voltage range leads to the variation of specific capacitance.[34] More interesting results obtained from the charge/discharge curves for VNN at different current densities (see Figure S3 in the Supporting Information). The fast fading of capacitance at higher current densities is due to pore resistance of porous network and solution resistance of the electrolyte (IR drop). At high current densities, IR drop is more and it decreases the specific capacitance values markedly, whereas at low current, the IR drop is negligible.[35]

The cyclic charge/discharge test is one of the important aspects to understanding the stability and service life of the capacitor for their practical applications. We have carried out the studies up to 600 cycles of charge/discharge for VNN electrode material to evaluate their stability as supercapacitor electrode material. Figure 6b reveals that the degradation in specific capacitance starts around 200 cycles. The insertion or deinsertion of electrolyte ions possibly induces a mechanical stress to the electrode active materials leads capacity fading.[36,37] The degradation continues for 100 cycles (up to 300 cycles). No further degradation could be observed beyond 300 cycles. Only around 24% loss was observed until 600 cycles. Lee et al. have reported $V_2O_5 \cdot nH_2O$ with around 45% degradation in the energy storage at 100 cycles.[38] Qu et, al. also have demonstrated degradation was observed after 100 cycles.[39] As compared to these reports the present materials especially VNN appears more efficient and exhibits longer cycling lifetime. This could be due to the interconnected network structure, which is good in withstanding the structural change during ion intercalation/de-intercalation.[40] One of the

important issues to answer for this technology is what directions will be important to enhance the energy density. The increasing of potential or capacitance leads to higher energy density.[41] It is worth mentioning that the highest energy density of 43.8 Wh kg^{-1} achieved for VNN. Perera et al., have reported energy density of 11.6 W h kg^{-1} for V_2O_5 nanotube spherical clusters in ionic liquid electrolyte.[42] Wee et al. have reported energy density of 5 W h kg^{-1} for V_2O_5 nanofibers in aqueous electrolyte.[43] V_2O_5 with nanoporous network morphology in the present work show a high energy density compared to the above reports. The energy density values for VNN3, VNN4, and VNN5 are 18.7, 13.2, and 12.5 W h kg^{-1}, respectively.

3.5.3. Influence of Morphology on Specific Capacitance. Capacitive properties also can be explained on the basis of surface morphology of all studied samples. From SEM, TEM, and pore size analysis, it is found that VNN sample carries interconnected nanoporous porous network morphology with mesopores. Presence of mesopores is highly favorable for achieving high specific capacitance. The nanoporous network configuration provides nanosized pathways and facilitates an effective electrolyte penetration. This creates more oxide-electrolyte interfaces for surface reactions. Because of this, the overall charge storage kinetics can be improved and highest specific capacitance 316 F g^{-1} was achieved for VNN samples and it is higher than values reported by others.[36,43,44] The morphology of VNN was destroyed by an increase in annealing temperature, which is confirmed by SEM and pore size analysis. The specific capacitance was found to decrease from 316 to 135 F g^{-1} for VNN3, which is attributed to shrinkage of porous morphology and lack of more facile sites for ion intercalation. Further, the increase in annealing temperature leads to decreasing specific capacitance.

3.5.4. Impedance Studies. The main objective of the electrochemical impedance spectroscopy (EIS) measurements is to gain insight of the resistive and capacitive elements associated with the electrode. Figure 7a shows Nyquist plot for VNN,VNN3,VNN4 and VNN5 in the frequency range of 0.01 Hz and 1 × 10^5 Hz. Nyquist plot is a plot of the imaginary component (Z'') of the impedance against the real component (Z'). The lower left portion of the curve corresponds to the higher frequencies. The Nyquist plot can be depicted by a modified Randles circuit as shown in Figure 7b. Ohmic resistance of the electrolyte and internal resistance of the electrode materials is denoted as R_S. The interfacial charge transfer resistance (R_{CT}) and double layer capacitance C_{DL} are parallely connected to represent the semicircle in the high frequency region. R_{CT} is measured by the intercept of the semi circle with the real axis (Z'). The determined R_{CT} values for VNN, VNN3, VNN4, and VNN5 are 5.85, 5.33, 4.9, and 4.77 Ω, respectively. Here we note that the charge transfer resistance, R_{CT}, decreases as the annealing temperature increases. It shows that the surface modification of the material also increasing the conductivity of the electrode materials.[45] An ideal polarizable capacitance shows the straight line parallel to the imaginary axis of the plot with mass capacitance (C_L) at low frequencies.[46] Here it is noted that the spectra inclined at an angle to the real axis, suggesting that a resistance is associated with C_L. This resistance is termed as leakage resistance (R_L) and connected parallel to C_L. The transition from high-frequency semicircle to low-frequency tail is represented by Warburg element (W).

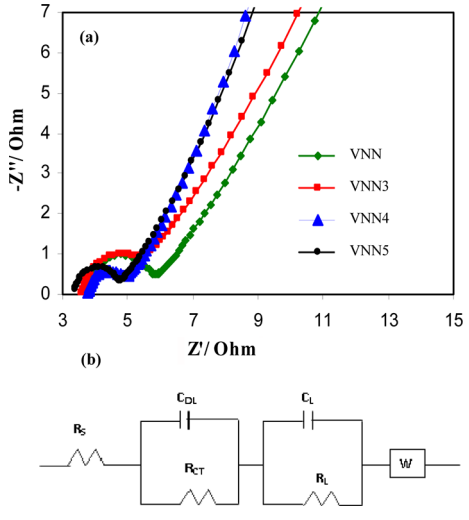

Figure 7. (a) Nyquist plot of VNN, VNN3, VNN4, and VNN5 electrodes. (b) Modified Randles circuit model.

3.6. Comparison of Present Work with Literature. The electrochemical performance of the VNN in the present study is compared with the literature reports. Number of investigations on V_2O_5 is quite less for supercapacitor applications exclusively. Reddy et al., demonstrated the high specific capacitance of 214 F g^{-1} in 2 M KCl at 5 mV s^{-1} for porous V_2O_5.[36] Hydrothermally prepared $V_2O_5{\cdot}0.6H_2O$ nanoribbons reported by Qu et al., were found to deliver maximum capacitance of 180.7 F g^{-1} with energy density of 29 W h kg^{-1}.[39] Wee et al., obtained V_2O_5 nanofibers using electrospinning followed by heat treatment at different temperatures. This material showed specific capacitance of 190 F g^{-1} in 2 M KCl electrolyte for the material annealed at 400 °C. The cycling performance of this material was not discussed by the authors.[43] Lao et al. have reported specific capacitance of 262 F g^{-1} in 2 M KCl at 5 mV s^{-1} for V_2O_5 powders with annealing temperature of 300 °C.[44] However most studies from the literature showed the highest specific capacitance achieved in higher annealing temperature with the use of relatively expensive laboratory equipments. The VNN in the present study delivered a superior specific capacitance value of 316 F g^{-1} in environmental friendly K_2SO_4 electrolyte with promising energy density of 43.8 W h kg^{-1}. This material also exhibits comparatively excellent capacity retention. Nanoporous structured V_2O_5 prepared in this study using simple chemical route showed an excellent capacity, energy density, and cyclic stability compared to other literature reports.

4. CONCLUSION

We have fabricated interconnected V_2O_5 nanoporous network and explored its electrochemical performance in K_2SO_4 aqueous electrolyte for supercpacitor application. The introduction of nanoporous network enhances the ion diffusion to the electrode material and lead to superior specific capacitance of 316 F g^{-1} and an energy density of 43.8 W h kg^{-1}. This high specific capacitance has been confirmed by low values of interfacial charge transfer resistance. The much improved specific capacitance, energy density, and stability of VNN ensured that the use of V_2O_5 nanoporous network for newly developed supercapacitors. The as prepared V_2O_5 exhibits better capacitance than those annealed at 300 °C or higher temperature.

■ ASSOCIATED CONTENT

Supporting Information

CV curves for all samples at 5 mV s^{-1}, anodic peak current dependence of scan rate from CV measurements, and charge/discharge curves for VNN measured at different current densities. This material is available free of charge via the Internet at http://pubs.acs.org./.

■ AUTHOR INFORMATION

Corresponding Author

*E-mail: muralg@rediffmail.com. Tel: +91451 2452371.

Notes

The authors declare no competing financial interest.

■ REFERENCES

(1) Simon, P.; Gogotsi, Y. *Nat. Mater.* **2008**, *20*, 845−854.
(2) Liu, C.; Yu, Z.; Neff, D.; Zhamu, A.; Jang, B. Z. *Nano Lett.* **2010**, *10*, 4863−4868.
(3) Mishra, A. K.; Ramaprabhu, S. J. *J. Phys. Chem. C* **2011**, *115* (29), 14006−14013.
(4) Khoo, E.; Wang, J. M.; Ma, J.; Lee, P. S. *J. Mater. Chem.* **2010**, *20*, 8368−8374.
(5) Mai, L.; Xu, L.; Han, C.; Xu, X.; Luo, Y.; Zhao, S.; Zhao, Y. *Nano Lett.* **2010**, *10*, 4750−4755.
(6) Doherty, C. M.; Caruso, R. A.; Smarsly, B. M.; Adelhelm, P.; Drummond, C. J. *Chem. Mater.* **2009**, *21*, 5300−5306.
(7) Chen, W.; Rakhi, R. B.; Hu, L.; Xie, X.; Cui, Y.; Alshareef, H. N. *Nano Lett.* **2011**, *11*, 5165−5172.
(8) Wu, D.; Hui, C. M.; Dong, H.; Pietrasik, J.; Ryu, H. J.; Li, Z.; Zhong, M.; He, H.; Kim, K.; Jaroniec, M.; Kowalewski, T.; Matyjaszewski, K. *Macromolecules* **2011**, *44*, 5846−5849.
(9) Zhao, X.; Mendoza, B.; Anchez, S.; Dobson, P. J.; Grant., P. S. *Nanoscale* **2011**, *3*, 839−855.
(10) Hu, C. C.; Chen, W. C. *Electrochim. Acta* **2004**, *49*, 3469−3477.
(11) Chen, S.; Zhu, J.; Wu, X.; Han, Q. F.; Wang., X. *ACS Nano* **2010**, *5*, 2822−2830.
(12) Lu, Z.; Chang, Z.; Liu, J.; Sun, X. *Nano Res.* **2011**, *4* (7), 658−665.
(13) Lang, J.; Yan, X.; Xue, Q. *J. Power Sources.* **2011**, *196*, 7841−7846.
(14) Whittingham, M. S. *J. Electrochem. Soc.* **1976**, *123*, 315−320.
(15) Rui, X; Zhu, J.; Liu, W.; Tan, H.; Sim, D.; Xu, C.; Zhang, H.; Ma, J.; Hng, H. H.; Lim, T. M.; Yan, Q. *RSC Adv.* **2011**, *1*, 117−122.
(16) Xiong, C.; Aliev, A. E.; Gnade, B.; Balkus, K. J. *ACS Nano* **2008**, *2*, 293−301.
(17) Yu, D.; Chen, C.; Xie, S.; Liu, Y.; Park, K.; Zhou, X.; Zhang, Q.; Lic, J.; Cao, G. *Energy Environ. Sci.* **2011**, *4*, 858−861.
(18) Li, M.; Kong, F.; Wang, H.; Li, G. *Cryst. Eng. Comm.* **2011**, *13*, 5317−5320.
(19) Chen, W.; Zhou, C.; Mai, L.; Liu, Y.; Qi, Y.; Dai, Y. *J. Phys. Chem. C.* **2008**, *112*, 2262−2265.
(20) Qu, Q. T.; Shi, Y.; Tian, S.; Chen, Y. H.; Wu, Y. P.; Holze, R. *J. Power Sources.* **2009**, *194*, 1222−1225.
(21) Qu, Q. T.; Zhang, P.; Wang, B.; Chen, Y.; Tian, S.; Wu, Y.; Holze., R. *J. Phys. Chem. C* **2009**, *113* (31), 14020−14027.
(22) Liu, Y.; Clark, M.; Zhang, Q.; Yu, D.; Liu, D.; Liu, J.; Cao, G. *Adv. Energy Mater.* **2011**, *1*, 194−202.
(23) Alonso, B.; Livage, J. *J. Solid State Chem.* **1999**, *148*, 16−19.
(24) Choi, J. W.; McDonough, J.; Jeong, S.; Yoo, J. S.; Chan, C. K.; Cui, Y. *Nano Lett.* **2010**, *10*, 1409−1413.
(25) Chen, Z.; Augustyn, V.; Wen, J.; Zhang, Y.; Shen, M.; Dunn, B.; Lu, Y. *Adv. Mater.* **2011**, *23*, 791−795.
(26) Ragupathy, P.; Shivakumara, S.; Vasan, H. N; Munichandraiah, N. *J. Phys. Chem. C.* **2008**, *112*, 16700−16707.
(27) Xiong, W.; Liu, M.; Gan, L.; Lv, Y.; Li, Y.; Yang, L.; Xu, Z.; Hao, Z.; Liu, H.; Chen., L. *J. Power Sources.* **2011**, *196*, 10461−10464.
(28) Meher, S. K.; Justin, P.; Rao, G. R. *J. Phys. Chem. C* **2010**, *11*, 5205−5210.
(29) Nayak, P. K.; Munichandraiah, N. *Microporous Mesoporous Mater.* **2011**, *143*, 206−214.
(30) Zhu, J.; He, J. *ACS Appl. Mater. Interfaces* **2012**, *4*, 1770−1776.
(31) Meher, S. K.; Justin, P.; Rao, G. R. *ACS Appl. Mater. Interfaces* **2011**, *3*, 2063−2073.
(32) Mai, L. Q.; Yang, F.; Zhao, Y. L.; Xu, X.; Xu, L.; Luo, Y. Z. *Nat. Commun.* **2011**, *2*, 381 DOI: 10.1038/ncomms1387.
(33) Yang, Y.; Kim, D.; Yang, M.; Schmuki, P. *Chem. Commun.* **2011**, *47*, 7746−7748.
(34) Kelly, T. L.; Yano, K.; Wolf, M. O. *ACS Appl. Mater. Interfaces* **2009**, *1* (11), 2536−2543.
(35) Meher, S. K.; Justin, P.; Rao, G. R. *Electrochim. Acta* **2010**, *55*, 8388−8396.
(36) Reddy, R. N.; Reddy, R. G. *J. Power Sources.* **2006**, *156*, 700−704.
(37) Wang, Y.; Takahashi, K.; Shang, H.; Cao, G. *J. Phys. Chem. B* **2005**, *109* (8), 3085−3088.
(38) Lee, H. Y.; Goodenough, J. B. *J. Solid State Chem.* **1999**, *148*, 81−84.
(39) Qu, Q. T.; Shi, Y.; Li, L. L.; Guo, W. L.; Wu, Y. P.; Zhang, H. P.; Guan, S. Y.; Holze, R. *Electrochem. Commun.* **2009**, *11*, 1325−1328.
(40) Meher, S. K.; Rao, G. R. *J. Power Sources.* **2012**, *215*, 317−328.
(41) Naoi, K. *Fuel Cells.* **2010**, *10*, 825−833.
(42) Perera, S. D.; Patel, B.; Bonso, J.; Grunewald, M.; Ferraris, J. P.; Balkus, K. J., Jr. *ACS Appl. Mater. Interface* **2011**, *3*, 4512−4517.
(43) Wee, G.; Soh, H. Z.; Cheah, Y. L.; Mhaisalkar, S. G.; Srinivasan, M. *J. Mater. Chem.* **2010**, *20*, 6720−6725.
(44) Lao, Z. J.; Konstantinov, K.; Tournaire, Y.; Ng, S. H.; Wang, G. X.; Liu, H. K. *J. Power Sources* **2006**, *162*, 1451−1454.
(45) Kim, T. Y.; Lee, H. W.; Stoller, M.; Dreyer, D. R.; Bielawski, C. W.; Ruoff, R. S; Suh, K. S. *ACS Nano* **2010**, *5*, 436−442.
(46) Masarapu, C.; Zeng, H. F.; Hung, K. H.; Wei, B. *ACS. Nano* **2009**, *3*, 2199−2206.